Holistic Small-Signal Modeling and AI-Assisted Region-Based Stability Analysis of Autonomous AC and DC Microgrids

Yuxi Men
College of Engineering
Temple University
Philadelphia, PA, USA
yuxi.men@temple.edu

Lizhi Ding
College of Engineering
Temple University
Philadelphia, PA, USA
lizhi.ding@temple.edu

Yuhua Du
College of Engineering
Temple University
Philadelphia, PA, USA
yuhua.du@temple.edu

Xiaonan Lu
College of Engineering
Temple University
Philadelphia, PA, USA
xiaonan.lu@temple.edu

Dongbo Zhao
Energy Systems Division
Argonne Nationa Laboratory
Lemont, IL, USA
dongbo.zhao@anl.gov

Yue Cao
School of Electrical Engineering
and Computer Science
Oregon State University
Corvallis, OR, USA
yue.cao@oregonstate.edu

***Abstract*—In this paper, a holistic small-signal model of hybrid AC and DC microgrids is developed, including AC subsection, DC subsection, and interface inverters between AC and DC buses. Based on the derived complete small-signal model, a region-based stability analysis approach is proposed and developed. Meanwhile, to obtain the steady-state operating points used in the region-based stability analysis, practical and effective power flow calculation is conducted for droop-controlled hybrid AC and DC microgrids. Rather than following a conventional point-by-point stability evaluation procedure, the stability region implemented in this work is derived based on the selected cross-domain parameters from either control systems or main power circuits. Furthermore, an artificial intelligence (AI) assisted Kernel Ridge Regression (KRR) algorithm is implemented to derive the stability boundary with enhanced computational efficiency. Simulation tests are presented to demonstrate the effectiveness of the proposed method.**

Keywords—Hybrid AC and DC Microgrids, Kernel Ridge Regression, Small-signal Stability, Stability Region

I. INTRODUCTION

Increasing penetration of inverter-based resources challenges modern distribution systems with insufficient inertia and increasing generation intermittency. To mitigate the impacts of operational uncertainties, the concept of microgrids (MGs) was proposed for effectively integrating distributed energy resources (DERs) and enhancing grid operational performance. In the past years, AC MGs have been extensively studied, given that conventional grids are implemented based upon AC electricity [1]. Meanwhile, with increasing penetration of DC-coupled resources (e.g., photovoltaics [PVs], battery energy storage, etc.), the technology frontier of DC MGs has been significantly advanced that enables a hybrid architecture with both AC and DC resources, i.e., hybrid AC and DC MGs [2].

Given that the DER interface inverters are commonly parallel-connected in MGs, effective controls play a vital role in MG operation, especially for proportional output power sharing among multiple inverters. Various control strategies have been developed to achieve accurate power sharing in MGs, including centralized control approaches (e.g., master-slave control [3], central current control [4], etc.), decentralized control (e.g., droop control [5], [6], virtual synchronous generators [7], etc.), and distributed control (e.g., hierarchical control [8], [9], consensus-based control [10]–[14], etc.), among which given the simplicity in implementation and the effectiveness, droop control is commonly used to achieve proper power sharing among DGs in MGs.

Note that hybrid AC and DC MGs have relatively complex operational dynamics due to the hybrid and inverter dominated configuration. Therefore, it is critical and also challenging for small-signal stability analysis compared to conventional power grids [15]. Meanwhile, it is worth mentioning that conventional small-signal stability analysis follows a point-by-point procedure, i.e., the derived small-signal models are only applicable at specific operating points. Therefore, for hybrid AC and DC MGs, considering the large-scale integration of inverter-based resources and the requirements of a scalable architecture, there are additional obstacles of deriving a holistic small-signal model of the entire system and conducting stability analysis accordingly. In [15], the small-signal modeling of a hybrid AC and DC MG is presented, focusing on AC MG, DC MG and interlink converters between common AC and DC buses. Meanwhile, synthetic droop characteristics for regulating interlink converters are implemented to control the power exchange between AC and DC MGs. In [16], the modeling and control of the inverter dominated AC MG is studied in detail to conduct small-signal analysis. In [17], a reduced-order model is

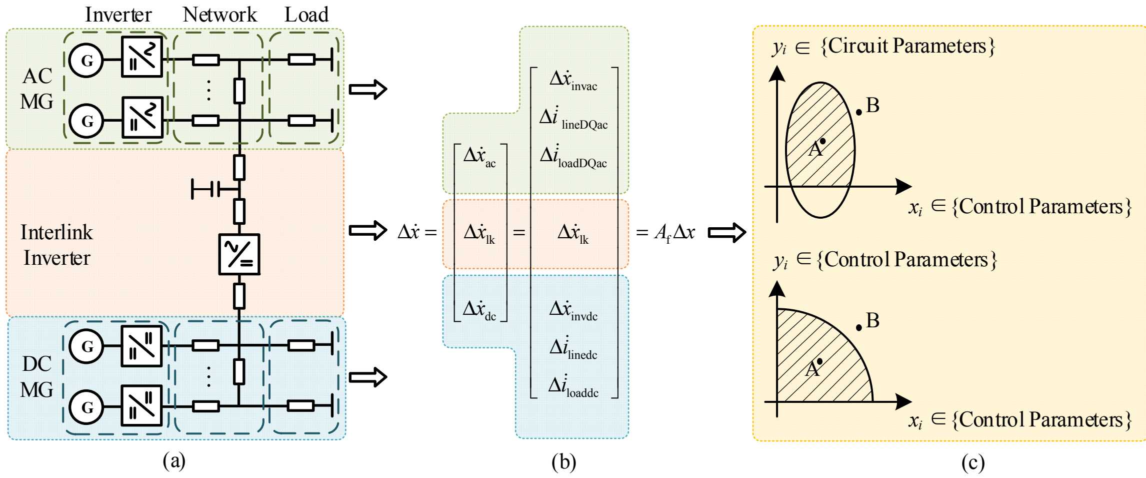

Fig. 1. Configuration of a typical autonomous AC and DC hybrid MG.
(a) System architecture; (b) Small-signal modeling of each subsection; (c) Stability region.

developed to analyze the stability of low-voltage DC MG. However, although the existing work has studied the small-signal models of different sections in hybrid AC and DC MGs, a complete solution covering various control functions (e.g., droop control, virtual impedance, etc.) and all the corresponding sections (i.e., AC section, DC section, and interface inverters between AC and DC buses) should be developed to derive a holistic model for stability analysis.

Given the complexity of small-signal models and the corresponding stability analysis of hybrid AC and DC MGs, it is necessary to develop an intuitive and computationally efficient approach that can identify system stability margin with real-time operating conditions. It is noteworthy that region-based stability was proposed and studied in transmission systems focusing on dynamic networks with multiple rotational generators [18]. The idea was originated from small-signal stability analysis while provided a stable region and depicted a stability margin based on the distance between the operating point and the region boundary. Rather than a point-by-point approach designed for each specific operating point, a stability region shows a feasible and stable operating range in a straight-forward way, focusing on the selected cross-domain parameters from the control diagram and main power circuit. However, considering that a hybrid AC and DC MG with multiple interface inverters is a high-order system, which is more complicated compared to conventional transmission grids, the applicability of the existing stability region should be further studied. Additionally, it should also be noted that deriving the stability region boundary is critical to implement a practical region-based stability analysis. Conventionally, the stability boundary is derived from exhausting the operating points with selected minimum steps [19], which could involve a tradeoff between the accuracy of the stability boundary and the required resolution. Therefore, a more efficient approach should be designed to simplify the procedure of identifying stability boundaries.

In this paper, to better understand the operation dynamics and the interactions among multiple sections, a holistic small-signal model of a hybrid AC and DC MG is derived, considering AC subsection, DC subsection, and interlink inverters in between. Furthermore, a region-based stability analysis is thereby conducted based on the derived holistic small-signal model and the selected cross-domain parameters from control diagram and main power circuit throughout the entire hybrid AC and DC MGs. Further, to efficiently and effectively derive the stability boundary, an Artificial Intelligence (AI) assisted approach is designed. Particularly, the Kernel Ridge Regression (KRR) approach is used to identify the stability region, which only relies on limited data points along the stability region and avoids the potential tradeoff between computational efficiency and required resolution.

The remainder of this paper is organized as follows: Section II introduces the small-signal modeling of droop-controlled autonomous AC and DC hybrid MGs. Section III studies the region-based stability analysis based on the KRR approach. Section IV presents two case studies on a hybrid AC and DC MG to verify the proposed solution. Section V summarizes the paper and draws the conclusion.

II. Small Signal Modeling of Hybrid AC/DC MGs

As depicted in Fig. 1 (a), a typical hybrid AC and DC MG includes AC MG, DC MG and interlink inverters between common AC and DC buses. Meanwhile, for both AC and DC subsections, they are separated into three segments, i.e., DER interface inverters, networks, and loads. The individual small-signal model of each section is detailed in this section, and the complete model of a hybrid AC and DC MG is derived by combining these individual models in Fig. 1 (b).

A. Modeling of DC Subsection

The entire DC MG is derived into three parts, i.e., interface converters, coupling lines connecting to the local point of interconnection (POI), and loads. The small-signal model of each part is derived, considering both control dynamics and main power circuits. Further, it is assumed that the DC MG is comprised of *s* converters, *n* lines, *m* buses, and *p* loads.

1) Interface DC-DC Converters: For the models of interface converters, the instantaneous active power in DC MGs is calculated by the measured output voltage and current.

Meanwhile, the corresponding average active power P_{dc} is obtained using a low-pass filter (LPF), as detailed below:

$$P_{dc} = \frac{\omega_c}{s+\omega_c} v_{odc}\, i_{odc} \tag{1}$$

where ω_c represents the cut-off frequency of low-pass filter; v_{odc} and i_{odc} are the converter output voltage and current.

Therefore, the small-signal representation of power control is derived:

$$\Delta\dot{P}_{dc} = -\omega_c \Delta P + \omega_c I_{odc} \Delta v_{odc} + \omega_c v_{odc} \Delta I_{odc} \tag{2}$$

The droop control at the DC side is realized as:

$$v_{odc} = V_{ndc} - m_{pdc} P_{dc} \tag{3}$$

where V_{ndc} is the reference of output voltage in DC subsection; m_{pdc} is the droop coefficient. Then the small-signal model of the output voltage is:

$$\Delta\dot{v}_{odc} = -m_{pdc} \Delta\dot{P}_{dc} \tag{4}$$

Furthermore, the interface converters in DC MGs connect to the local buses through the coupling inductance L_{cdc}, and virtual impedance (i.e., R_{vdc} + jωL_{vdc}) is added to the corresponding converter control diagram. Hence, it yields:

$$\Delta\dot{i}_{odc} = \frac{1}{L_{cdc}+L_{vdc}}(\Delta v_{odc} - v_{bdc}) - \frac{R_{cdc}+R_{vdc}}{L_{cdc}+L_{vdc}} \Delta i_{odc} \tag{5}$$

where Δv_{bdc} is the small-signal representation of bus voltage.

For the i^{th} DC-DC converter, combining (2), (4) and (5), for each interface converter, there are three state variables in total (i.e., ΔP_{dci}, Δv_{odci}, and Δi_{odci}) in the vector of state variables (Δx_{invdci}) with small-signal representation, defined as:

$$\begin{aligned} [\Delta\dot{x}_{invdci}] &= A_{invdci}[\Delta x_{invdci}] + B_{invdci}[\Delta v_{bdci}] \\ [\Delta i_{odci}] &= C_{invdci}[\Delta x_{invdci}] \end{aligned} \tag{6}$$

where

$$A_{invdci} = \begin{bmatrix} -\omega_c & \omega_c I_{odc} & \omega_c V_{odc} \\ m_{pdc}\omega_c & -m_{pdc}\omega_c I_{odc} & -m_{pdc}\omega_c V_{odc} \\ 0 & \frac{1}{L_{cdc}+L_{vdc}} & \frac{-(R_{cdc}+R_{vdc})}{L_{cdc}+L_{vdc}} \end{bmatrix} \quad B_{invdci} = \begin{bmatrix} 0 \\ 0 \\ \frac{-1}{L_{cdc}+L_{vdc}} \end{bmatrix}$$

$C_{invdci} = \begin{bmatrix} 0 & 0 & 1 \end{bmatrix}$.

Hence, based on (6), a combined small-signal model of all the DC-DC converters (s converters in total) is represented as:

$$\begin{aligned} [\Delta\dot{x}_{invdc}] &= A_{invdc}[\Delta x_{invdc}] + B_{invdc}[\Delta v_{bdc}] \\ [\Delta i_{odc}] &= C_{invdc}[\Delta x_{invdc}] \end{aligned} \tag{7}$$

where

$A_{invdc} = \text{diag}\{[A_{invdc1} \cdots A_{invdcs}]\}$ $\quad B_{invdc} = \text{diag}\{[B_{invdc1} \cdots B_{invdcs}]\}$

$C_{invdc} = \text{diag}\{[C_{invdc1} \cdots C_{invdcs}]\}$.

2) DC Network and Load Models: The power lines (n lines, m buses, and p loads) in the DC subsection are modeled as the combination of series resistance R_{lineac} and inductance L_{linedc}.

$$[\Delta\dot{i}_{linedc}] = A_{netdc}[\Delta i_{linedc}] + B_{netdc}[\Delta v_{bdc}] \tag{8}$$

where

$$A_{netdc} = \begin{bmatrix} \frac{-R_{linedc1}}{L_{linedc1}} & & \\ & \ddots & \\ & & \frac{-R_{linedcn}}{L_{linedcn}} \end{bmatrix}_{n\times n} \quad B_{netdc} = \begin{bmatrix} \frac{1}{L_{linedc1}} & \frac{-1}{L_{linedc1}} & & \\ & \ddots & \ddots & \\ & & \frac{1}{L_{linedcn}} & \frac{-1}{L_{linedcn}} \end{bmatrix}_{n\times m}.$$

For loads in DC MG, the small-signal models are derived:

$$[\Delta\dot{i}_{loaddc}] = A_{loaddc}[\Delta i_{loaddc}] + B_{loaddc}[\Delta v_{bdc}] \tag{9}$$

where

$$A_{loaddc} = \begin{bmatrix} \frac{-R_{loaddc1}}{L_{loaddc1}} & & \\ & \ddots & \\ & & \frac{-R_{loaddcp}}{L_{loaddcp}} \end{bmatrix}_{p\times p} \quad B_{loaddc} = \begin{bmatrix} \frac{1}{L_{loaddc1}} & & \\ & \ddots & \\ & & \frac{1}{L_{loaddcm}} \end{bmatrix}_{p\times m}.$$

3) Complete Model of DC Subsection: It is defined that M_{invdc}, M_{netdc}, and M_{loaddc} are the mapping matrices among inverters, lines, and loads. For example, M_{invdc} maps the inverter POIs onto the corresponding network buses. Hence, the DC bus voltage can be expressed below:

$$[\Delta v_{bdc}] = R_{Ndc}(M_{invdc}[\Delta i_{odc}] + M_{netdc}[\Delta i_{linedc}] + M_{loaddc}[\Delta i_{loaddc}]) \tag{10}$$

where

$R_{Ndc} = \text{diag}\{[r_N \cdots r_N]\}_{m\times m}$ $\quad M_{invdc} = \text{diag}\{[1 \cdots 1]\}_{m\times s}$

$$M_{netdc} = \begin{bmatrix} -1 & & \\ 1 & \ddots & \\ & \ddots & -1 \\ & & 1 \end{bmatrix}_{m\times n} \quad M_{loaddc} = \begin{bmatrix} -1 & & \\ & \ddots & \\ & & -1 \end{bmatrix}_{m\times p}.$$

Note that r_N is a large virtual resistance connecting the bus and ground, involved to satisfy the required number of equations [16].

Combining (7)–(10), the complete small-signal model of DC subsection is derived:

$$[\Delta\dot{x}_{dc}] = [\Delta\dot{x}_{invdc} \quad \Delta\dot{i}_{linedc} \quad \Delta\dot{i}_{loaddc}]^T = A_{dc}[\Delta x_{dc}] \tag{11}$$

where the state matrix A_{dc} of the DC subsection is given at the bottom of this page.

B. Modeling of AC Subsection

Similar to the DC subsection, the main components in the AC subsection include three parts (i.e., interface inverters, lines, and loads). The small-signal modeling of each part is presented as follows separately. Meanwhile, it is also assumed that the AC MG consists of s inverters, n lines, m buses, and p loads.

1) Interface Inverters: For the model of inverters, the average active power P_{ac} and reactive power Q_{ac} are derived as:

$$A_{dc} = \begin{bmatrix} A_{invdc} + B_{invdc}R_{Ndc}M_{invdc}C_{invdc} & B_{invdc}R_{Ndc}M_{netdc} & B_{invdc}R_{Ndc}M_{loaddc} \\ B_{netdc}R_{Ndc}M_{invdc}C_{invdc} & A_{netdc} + B_{netdc}R_{Ndc}M_{netdc} & B_{netdc}R_{Ndc}M_{loaddc} \\ B_{loaddc}R_{Ndc}M_{invdc}C_{invdc} & B_{loaddc}R_{Ndc}M_{netdc} & A_{loaddc} + B_{loaddc}R_{Ndc}M_{loaddc} \end{bmatrix}$$

$$P_{\mathrm{ac}} = \frac{\omega_{\mathrm{c}}}{s+\omega_{\mathrm{c}}}(v_{\mathrm{odac}} i_{\mathrm{odac}} + v_{\mathrm{oqac}} i_{\mathrm{oqac}})$$
$$Q_{\mathrm{ac}} = \frac{\omega_{\mathrm{c}}}{s+\omega_{\mathrm{c}}}(v_{\mathrm{oqac}} i_{\mathrm{odac}} - v_{\mathrm{odac}} i_{\mathrm{oqac}}) \tag{12}$$

Furthermore, each inverter follows the conventional *P–f* and *Q–V* droop characteristics to achieve power sharing among multiple inverters, as shown in (13):

$$\begin{aligned} \omega &= \omega_{\mathrm{n}} - m_{\mathrm{pac}} P_{\mathrm{ac}} \\ v_{\mathrm{odac}} &= V_{\mathrm{nac}} - n_{\mathrm{qac}} Q_{\mathrm{ac}} \\ v_{\mathrm{oqac}} &= 0 \end{aligned} \tag{13}$$

where ω_{n} is the nominal frequency; V_{nac} is the reference of output voltage in the AC side; m_{pac} and n_{qac} are droop gains.

Since an individual *dq* frame is used for each inverter, multiple *dq* frames can be synchronized and converted into a common frame [16]. In general, the *dq* frame of the first interface inverter is selected as the common *DQ* frame. The phase angle difference between an inverter and the common *DQ* frame is represented as:

$$\delta_{\mathrm{ac}} = \int (\omega - \omega_{\mathrm{com}})\mathrm{dt} \tag{14}$$

where ω_{com} is the angular frequency of the common *DQ* frame.

Similar to the DC subsection, the state equation of inverter output current i_{odqac} is derived since each inverter connects to a local bus through a coupling inductance L_{cac}. Additionally, the virtual impedance (i.e., $R_{\mathrm{vac}}+ \mathrm{j}\omega L_{\mathrm{vac}}$) is added to the model.

$$\dot{i}_{\mathrm{odqac}} = \frac{(v_{\mathrm{odqac}} - v_{\mathrm{bdqac}})}{L_{\mathrm{cac}} + L_{\mathrm{vac}}} - \frac{R_{\mathrm{cac}} + R_{\mathrm{vac}}}{L_{\mathrm{cac}} + L_{\mathrm{vac}}} i_{\mathrm{odqac}} \pm \omega i_{\mathrm{oqdac}} \tag{15}$$

Meanwhile, with the synchronized frames and the derived phase angle difference in (14), the inverter output current i_{odqac} and bus voltage v_{bdqac} can be transferred to the corresponding i_{oDQac} and v_{bDQac} in the common *DQ* frame, respectively.

For the i^{th} inverter, similar to the small-signal modeling of DC section, by linearizing (12)–(15), there are seven state variables (i.e., $\Delta\delta_{\mathrm{ac}i}$, $\Delta P_{\mathrm{ac}i}$, $\Delta Q_{\mathrm{ac}i}$, $\Delta v_{\mathrm{odqac}i}$, and $\Delta i_{\mathrm{odqac}i}$) in the state vector $x_{\mathrm{invac}i}$ for one interface inverter in AC MGs.

$$\begin{aligned} [\Delta\dot{x}_{\mathrm{invac}i}] &= A_{\mathrm{invac}i}[\Delta x_{\mathrm{invac}i}] + B_{\mathrm{invac}i}[\Delta v_{\mathrm{bDQac}i}] + B_{\omega\mathrm{com}i}[\Delta\omega_{\mathrm{com}}] \\ \begin{bmatrix} \Delta\omega_i \\ \Delta i_{\mathrm{oDQac}i} \end{bmatrix} &= \begin{bmatrix} C_{\mathrm{inv}\omega\mathrm{ac}i} \\ C_{\mathrm{invcac}i} \end{bmatrix} [\Delta x_{\mathrm{invac}i}] \end{aligned} \tag{16}$$

where $A_{\mathrm{invac}i}$, $B_{\mathrm{invac}i}$, $B_{\mathrm{com}i}$, $C_{\mathrm{inv}\omega\mathrm{ac}i}$, and $C_{\mathrm{invcac}i}$ are given at the bottom of this page.

Therefore, a comprehensive small-signal model of all the *s* interface inverters derived as:

$$\begin{aligned} [\Delta\dot{x}_{\mathrm{invac}}] &= A_{\mathrm{invac}}[\Delta x_{\mathrm{invac}}] + B_{\mathrm{invac}}[\Delta v_{\mathrm{bDQac}}] \\ [\Delta i_{\mathrm{oDQac}}] &= C_{\mathrm{invcac}}[\Delta x_{\mathrm{invac}}] \end{aligned} \tag{17}$$

where

$$A_{\mathrm{invac}} = \begin{bmatrix} A_{\mathrm{invac1}} + B_{\omega\mathrm{com1}} C_{\mathrm{inv}\omega\mathrm{ac1}} & & & \\ B_{\omega\mathrm{com2}} C_{\mathrm{inv}\omega\mathrm{ac1}} & A_{\mathrm{invac2}} & & \\ \vdots & & \ddots & \\ B_{\omega\mathrm{com}s} C_{\mathrm{inv}\omega\mathrm{ac1}} & & & A_{\mathrm{invac}s} \end{bmatrix}$$

$$B_{\mathrm{invac}} = \mathrm{diag}\{[B_{\mathrm{invac1}} \cdots B_{\mathrm{invac}s}]\} \quad C_{\mathrm{invcac}} = \mathrm{diag}\{[C_{\mathrm{invcac1}} \cdots C_{\mathrm{invcac}s}]\}.$$

2) AC Network and Load Models: For the line and load currents, their state equations are similar to those in the DC subsection, while the state variables in the dq frame need to be transferred to the common DQ frame, as derived below:

$$[\Delta\dot{i}_{\mathrm{lineDQac}}] = A_{\mathrm{netac}}[\Delta i_{\mathrm{lineDQac}}] + B_{1\mathrm{netac}}[\Delta v_{\mathrm{bDQac}}] + B_{2\mathrm{netac}}\Delta\omega \tag{18}$$

$$[\Delta\dot{i}_{\mathrm{loadDQac}}] = A_{\mathrm{loadac}}[\Delta i_{\mathrm{loadDQac}}] + B_{1\mathrm{loadac}}[\Delta v_{\mathrm{bDQac}}] + B_{2\mathrm{loadac}}\Delta\omega \tag{19}$$

where coefficient matrices A_{netac}, $B_{1\mathrm{netac}}$, $B_{2\mathrm{netac}}$, A_{loadac}, $B_{1\mathrm{loadac}}$, and $B_{2\mathrm{loadac}}$ have a similar representation as those of DC lines and loads in (8)–(9).

3) Complete Model for AC Subsection: Similar to the DC MG, mapping matrices are defined to show the representation of AC bus voltage, as derived below. Meanwhile, the matrix R_{Nac} composed of a large virtual resistance r_{N} is involved in satisfying the equation set mathematically.

$$\begin{aligned} [\Delta v_{\mathrm{bDQac}}] = R_{\mathrm{Nac}}(M_{\mathrm{invac}}[\Delta i_{\mathrm{oDQac}}] &+ M_{\mathrm{loadac}}[\Delta i_{\mathrm{loadDQac}}] \\ &+ M_{\mathrm{netac}}[\Delta i_{\mathrm{lineDQac}}]) \end{aligned} \tag{20}$$

Hence, combining (17)–(20), the complete small-signal state-space model of the AC MG is summarized as:

$$[\Delta\dot{x}_{\mathrm{ac}}] = [\Delta\dot{x}_{\mathrm{invac}} \quad \Delta\dot{i}_{\mathrm{lineDQac}} \quad \Delta\dot{i}_{\mathrm{loadDQac}}]^{\mathrm{T}} = A_{\mathrm{ac}}[\Delta x_{\mathrm{ac}}] \tag{21}$$

$$A_{\mathrm{invac}i} = \begin{bmatrix} 0 & -m_{\mathrm{pac}} & 0 & 0 & 0 & 0 & 0 \\ 0 & -\omega_{\mathrm{c}} & 0 & \omega_{\mathrm{c}} I_{\mathrm{od}} & \omega_{\mathrm{c}} I_{\mathrm{oqac}} & \omega_{\mathrm{c}} V_{\mathrm{odac}} & \omega_{\mathrm{c}} V_{\mathrm{oqac}} \\ 0 & 0 & -\omega_{\mathrm{c}} & -\omega_{\mathrm{c}} I_{\mathrm{oqac}} & \omega_{\mathrm{c}} I_{\mathrm{odac}} & \omega_{\mathrm{c}} V_{\mathrm{oqac}} & -\omega_{\mathrm{c}} V_{\mathrm{odac}} \\ 0 & 0 & n_{\mathrm{qac}}\omega_{\mathrm{c}} & n_{\mathrm{qac}}\omega_{\mathrm{c}} I_{\mathrm{oqac}} & -n_{\mathrm{qac}}\omega_{\mathrm{c}} I_{\mathrm{odac}} & -n_{\mathrm{qac}}\omega_{\mathrm{c}} V_{\mathrm{oqac}} & n_{\mathrm{qac}}\omega_{\mathrm{c}} V_{\mathrm{odac}} \\ 0 & 0 & 0 & 0 & 0 & 0 & 0 \\ \frac{V_{\mathrm{bDac}}\sin\delta_0 - V_{\mathrm{bQac}}\cos\delta_0}{L_{\mathrm{cac}} + L_{\mathrm{vac}}} & -m_{\mathrm{pac}} I_{\mathrm{oqac}} & 0 & 1/L_{\mathrm{cac}} & 0 & \frac{-(R_{\mathrm{cac}} + R_{\mathrm{vac}})}{L_{\mathrm{cac}} + L_{\mathrm{vac}}} & \omega_0 \\ \frac{V_{\mathrm{bDac}}\cos\delta_0 + V_{\mathrm{bQac}}\sin\delta_0}{L_{\mathrm{cac}} + L_{\mathrm{vac}}} & m_{\mathrm{pac}} I_{\mathrm{odac}} & 0 & 0 & 1/L_{\mathrm{cac}} & -\omega_0 & \frac{-(R_{\mathrm{cac}} + R_{\mathrm{vac}})}{L_{\mathrm{cac}} + L_{\mathrm{vac}}} \end{bmatrix} \quad B_{\mathrm{invac}i} = \begin{bmatrix} 0 & 0 \\ \vdots & \vdots \\ 0 & 0 \\ \frac{-\cos\delta_0}{L_{\mathrm{cac}} + L_{\mathrm{vac}}} & \frac{-\sin\delta_0}{L_{\mathrm{cac}} + L_{\mathrm{vac}}} \\ \frac{\sin\delta_0}{L_{\mathrm{cac}} + L_{\mathrm{vac}}} & \frac{-\cos\delta_0}{L_{\mathrm{cac}} + L_{\mathrm{vac}}} \end{bmatrix}$$

$$B_{\omega\mathrm{com}i} = [-1\ 0 \cdots 0]^{\mathrm{T}} \qquad C_{\mathrm{inv}\omega\mathrm{ac}i} = \begin{cases} [0\ -m_{\mathrm{pac}}\ 0 \cdots 0] & i = 1 \\ [0 \cdots 0] & i \neq 1 \end{cases} \qquad C_{\mathrm{invcac}i} = \begin{bmatrix} -I_{\mathrm{odac}}\sin\delta_0 - I_{\mathrm{oqac}}\cos\delta_0 & 0 \cdots 0 & \cos\delta_0 & -\sin\delta_0 \\ I_{\mathrm{odac}}\cos\delta_0 - I_{\mathrm{oqac}}\sin\delta_0 & 0 \cdots 0 & \sin\delta_0 & \cos\delta_0 \end{bmatrix}$$

where the state matrix A_{ac} of the AC subsection is given at the bottom of this page.

C. Modeling of Interlink Inverters between AC and DC Buses

To satisfy the operating conditions in both AC and DC MGs, a *V–P* droop control is used at the DC side for each interlink inverter, which is aligned with other sources at the DC MG, as shown below:

$$v^{*}_{\mathrm{lk\_dc}} = V_{\mathrm{ndc}} - m_{\mathrm{lk}} P_{\mathrm{lk\_dc}} \tag{22}$$

where m_{lk} is the droop coefficient;

To smooth power exchange between AC and DC subsections, at the DC side of the interlink inverter, DC-link voltage is controlled to balance the active power while reactive power is controlled at the AC side locally. Thus, the average active power at the DC side and the average reactive power at the AC side are calculated as:

$$\begin{aligned} P_{\mathrm{lk\_dc}} &= \frac{\omega_c}{s+\omega_c} v_{\mathrm{lk\_dc}} i_{\mathrm{lk\_dc}} \\ Q_{\mathrm{lk\_ac}} &= \frac{\omega_c}{s+\omega_c} (v_{\mathrm{oqlk\_ac}} i_{\mathrm{odlk\_ac}} - v_{\mathrm{odlk\_ac}} i_{\mathrm{oqlk\_ac}}) \end{aligned} \tag{23}$$

A multi-loop control diagram is utilized in interlink inverters. Particularly, the outer control diagram includes DC-link voltage and reactive power control loops, and the inner control diagram includes the proportional-integral (PI) based current control loops, which is used to calculate the interlink inverter output voltage $v_{\mathrm{odqlk\_ac}}$ at the AC side.

Furthermore, the power balance between the AC and DC sides of the interlink inverter is derived below based on the power balance across the interlink inverter.

$$\begin{aligned} p_{\mathrm{lk\_ac}} &= -p_{\mathrm{lk\_dc}} \cdot \eta \\ v_{\mathrm{odlk\_ac}} i_{\mathrm{odlk\_ac}} + v_{\mathrm{oqlk\_ac}} i_{\mathrm{oqlk\_ac}} &= -v_{\mathrm{lk\_dc}} (i_{\mathrm{lk\_dc}} + C_{\mathrm{lk\_dc}} \dot{v}_{\mathrm{lk\_dc}}) \cdot \eta \end{aligned} \tag{24}$$

where v_{odqlk} and i_{odqlk} are the interlink inverter output voltage and current in *dq* reference frame, respectively; $C_{\mathrm{lk\_dc}}$ is the filter capacitor at the DC side of the interlink converter; η is the efficiency of interlink inverter.

Meanwhile, the DC side of interlink inverter connects to the DC bus using the coupling inductance $L_{\mathrm{clk\_dc}}$:

$$\dot{i}_{\mathrm{lk\_dc}} = \frac{1}{L_{\mathrm{clk\_dc}}} (v_{\mathrm{lk\_dc}} - v_{\mathrm{blk\_dc}}) - \frac{R_{\mathrm{clk\_dc}}}{L_{\mathrm{clk\_dc}}} i_{\mathrm{lk\_dc}} + \omega i_{\mathrm{lk\_dc}} \tag{25}$$

On the other hand, considering the LC filter and the coupling impedance ($R_{\mathrm{clk\_ac}}$, $L_{\mathrm{clk\_ac}}$) between the interlink inverter and local AC bus, the following state equations with the state variables i_{odqlk}, v_{dqlk} and i_{dqlk} are derived:

$$\dot{v}_{\mathrm{dqlk\_ac}} = \frac{1}{C_f} (i_{\mathrm{dqlk\_ac}} - i_{\mathrm{odqlk\_ac}}) \pm \omega v_{\mathrm{qdlk\_ac}} \tag{26}$$

where the $v_{\mathrm{dqlk\_ac}}$ is the voltage of capacitor C_f at the AC side of interlink inverter; Developing the state equations of $i_{\mathrm{odqlk\_ac}}$ and $i_{\mathrm{dqlk\_ac}}$ are similar to those of DC coupling inductance in (25).

Finally, considering the angle difference δ_{lk} between the interlink inverter and the common DQ frame, the local AC bus voltage $v_{\mathrm{bdqlk\_ac}}$ connecting the AC side of the interlink inverter and the corresponding injected current $i_{\mathrm{dqlk\_ac}}$ can be transferred to the common DQ frame, respectively.

Combining (22)–(26), there are 13 state variables in total, including $\Delta\delta_{lk}$, $\Delta P_{\mathrm{lk\_dc}}$, $\Delta Q_{\mathrm{lk\_ac}}$, $\Delta v_{\mathrm{odqlk\_ac}}$, $\Delta i_{\mathrm{odqlk\_ac}}$, $\Delta v_{\mathrm{dqlk\_ac}}$, $\Delta i_{\mathrm{dqlk\_ac}}$, $\Delta v_{\mathrm{lk\_dc}}$, and $\Delta i_{\mathrm{lk\_dc}}$ for an interlink inverter. The corresponding small-signal representation is thereby obtained:

$$\left[\Delta \dot{x}_{\mathrm{lk}}\right] = A_{\mathrm{lk}} \left[\Delta x_{\mathrm{lk}}\right] \tag{27}$$

where A_{lk} is the state matrix of the interlink inverter.

D. Complete Model of Hybrid AC and DC MGs

Based on the small-signal models derived in Section II-A to II-C, combining (11), (21) and (27), a complete small-signal model of an autonomous AC and DC hybrid MG is obtained:

$$[\Delta \dot{x}] = \left[\Delta \dot{x}_{\mathrm{ac}} \;\; \Delta \dot{x}_{\mathrm{lk}} \;\; \Delta \dot{x}_{\mathrm{dc}}\right]^{\mathrm{T}} = A_f [\Delta x] \tag{28}$$

where A_f is the coefficient matrix of the entire hybrid AC and DC MG; $B_{\mathrm{ac\_lk}}$, $B_{\mathrm{dc\_lk}}$, $B_{\mathrm{lk\_ac1}}$, $B_{\mathrm{lk\_ac2}}$, $B_{\mathrm{lk\_dc1}}$, and $B_{\mathrm{lk\_dc2}}$ are coupling elements among the AC MG, DC MG, and interlink inverters.

$$A_f = \begin{bmatrix} A_{\mathrm{ac}} & B_{\mathrm{ac\_lk}} & 0 \\ B_{\mathrm{lk\_ac1}} & A_{\mathrm{lk}} + B_{\mathrm{lk\_ac2}} + B_{\mathrm{lk\_dc2}} & B_{\mathrm{lk\_dc1}} \\ 0 & B_{\mathrm{dc\_lk}} & A_{\mathrm{dc}} \end{bmatrix}.$$

III. Region-Based Stability Analysis

Based on the small-signal model in (28), a stability region can be derived to evaluate system stability and identify small-signal stability margin. It is noteworthy that the stability region is defined and established based upon a parameter space with cross-domain parameters from control diagrams and main power circuits. As depicted in Fig. 1 (c), a selected point inside the stability region indicates that the system is stable with the given parameters while the system is unstable if a selected point is outside the stability region. The boundary of the stability region represents a marginally stable condition. Note that a stability region can be flexibly established with different combinations of control or main power circuit parameters. For example, it can be used to identify the interactions between two key control parameters (e.g., virtual impedance and droop coefficient), or quantify the impacts of parameter mismatch of passive components in main power circuits (e.g., filter inductance and capacitance). Therefore, region-based stability analysis can be regarded as a versatile solution to study various stability-related problems.

It is worth mentioning that the stability region boundary is derived using an AI-assisted regression algorithm, i.e., Kernel Ridge Regression (KRR). The stability boundary can be thereby derived based on only some sample points located along the region boundary rather than point-by-point with every parameter

$$A_{\mathrm{ac}} = \begin{bmatrix} A_{\mathrm{invac}} + B_{\mathrm{invac}} R_{\mathrm{Nac}} M_{\mathrm{invac}} C_{\mathrm{invcac}} & B_{\mathrm{invac}} R_{\mathrm{Nac}} M_{\mathrm{netac}} & B_{\mathrm{invac}} R_{\mathrm{Nac}} M_{\mathrm{loadac}} \\ B_{\mathrm{1netac}} R_{\mathrm{Nac}} M_{\mathrm{invac}} C_{\mathrm{invcac}} + B_{\mathrm{2netac}} C_{\mathrm{inv\omega ac}} & A_{\mathrm{netac}} + B_{\mathrm{1netac}} R_{\mathrm{Nac}} M_{\mathrm{netac}} & B_{\mathrm{1netac}} R_{\mathrm{Nac}} M_{\mathrm{loadac}} \\ B_{\mathrm{1loadac}} R_{\mathrm{Nac}} M_{\mathrm{invac}} C_{\mathrm{invac}} + B_{\mathrm{2loadac}} C_{\mathrm{inv\omega ac}} & B_{\mathrm{1loadac}} R_{\mathrm{Nac}} M_{\mathrm{netac}} & A_{\mathrm{loadac}} + B_{\mathrm{1loadac}} R_{\mathrm{Nac}} M_{\mathrm{loadac}} \end{bmatrix}$$

combination considered. The detailed design procedure is summarized in the flow chart in Fig. 2. Particularly, there are three main steps in the KRR method: data set generation, stability region boundary approximation, and KRR-based performance evaluation.

A. Dataset Generation

As depicted in Fig. 2, taking a parameter space $X = \{x_1, x_2\}$ as an example, an initial stable operating point $X_0 = \{x_{1\_0}, x_{2\_0}\}$ in the parameter space is selected, and starting from this point, a sampling direction d is determined to identify stability region boundary, where n_d is the total number of sampling directions and Δx_d is sampling intervals. Note that the maximum real part of the system eigenvalue σ_{max} is the critical variable to determine if the stability boundary is reached. When σ_{max} is less than 0, the corresponding parameter combination in the sampling direction leads to a stable operation condition; when it is larger than 0, the corresponding parameter combination indicates an unstable condition. Therefore, the stability boundary is identified when σ_{max} first changes to a positive value, and when the boundary is reached in the sampling direction d, the corresponding parameter combination $\{x_{1b}, x_{2b}\}$ is collected into the generated dataset for the following KRR stage. Further, given that it is challenging or even infeasible to derive $\{x_{1b}, x_{2b}\}$ with σ_{max} equals 0, an interval of σ_{max} is involved in tolerating the potential mismatch in the searching process. Here, the samples within the range of $[\delta_1, \delta_2]$ = [-0.2, 0] are preserved to enhance the resolution along the stability region boundary, while samples in the remaining area are selected with a sparse density. Therefore, the dataset of parameter space X can be obtained, and it is further divided into a training set and a validation set for the following KRR stage. Since there is no practical experience to follow and determine the capacities of the training set and the validation set, the generated dataset can be split into two randomly selected sets whose capacities are 50% of the original dataset.

It is worth mentioning that to calculate σ_{max}, system steady-state operating points are needed. Therefore, as shown as one step in the flow chart in Fig. 2, power flow calculation in hybrid AC and DC MGs should be conducted. Particularly, compared to the conventional Newton Raphson method in power flow analysis, a practical and effective modified Newton Raphson (MNR) approach [20] is used for power flow calculation in this study. For the MNR approach, due to the absence of the slack bus in an autonomous MG, Bus #1 with droop control is selected as the voltage reference in the power flow calculation. Meanwhile, the system angular frequency ω is also taken as another unknown variable since it is not a constant in droop-control MGs. Further, the droop-controlled buses at the AC and DC sides are formulated as:

$$P_{kac}^{i+1} = \frac{(\omega_0 - \omega^i)}{m_{pack}} \qquad Q_{kac}^{i+1} = \frac{(|V_0| - |V_{ack}^i|)}{n_{qack}} \qquad P_{kdc}^{i+1} = \frac{(|V_0| - |V_{dck}^i|)}{m_{pdck}} \tag{29}$$

where P_{kac} and Q_{kac} are the active and reactive powers of the droop- controlled k^{th} bus at the AC side; P_{kdc} is the output power of the droop-controlled k^{th} bus at the DC side.

In this study, to combine the power flow in the entire hybrid system, the interlink inverter is used as the bridge to satisfy the power flow calculation in both AC and DC subsections.

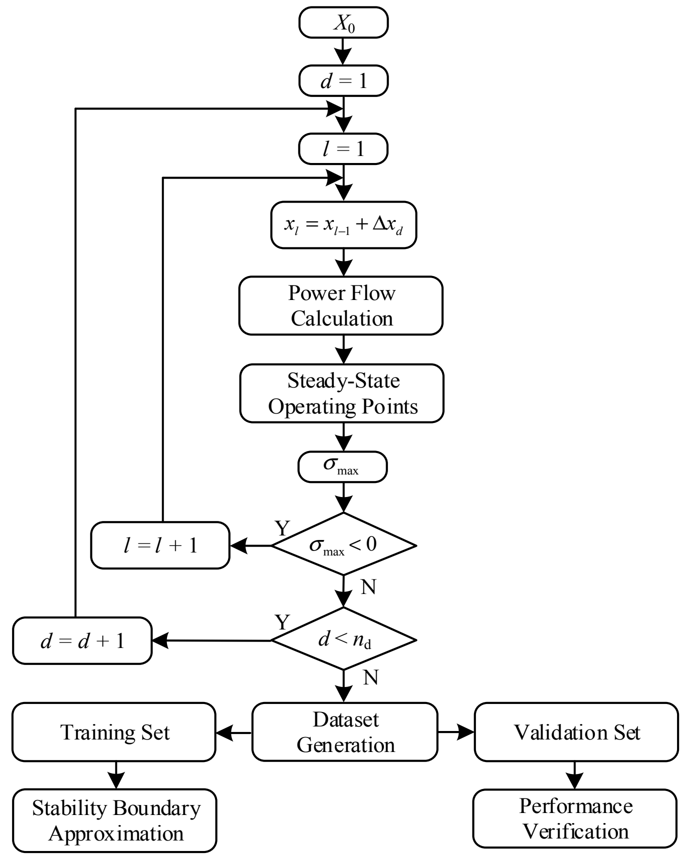

Fig. 2. Flow chart of KRR method for deriving the stability region boundary.

Particularly, as shown in (24), at the DC side, the interlink inverter is modeled as a droop-controlled bus; since power is balanced in both AC and DC sides, the active power at the AC side is determined by the calculated DC power, and the reactive power at the AC side is controlled locally (e.g., set to zero). Therefore, after modeling the interlink inverters, the power flow calculation in hybrid AC and DC MGs can be implemented following a two-step procedure. In Step 1, the power flow can be calculated in the DC subsection; in Step 2, given the above interlink inverter model, active power flowing through the interlink inverter is used as the shared variable, and power flow in the AC subsection can be thereby derived.

B. Stability Boundary Approximation

There exists a mapping function $f(\cdot)$ that links a parameter combination x to the corresponding stability index σ_{max}. This function $f(\cdot)$ represents the target stability region boundary, which can be derived using the KRR approach based on the sample points in the training dataset.

However, $f(x) = 0$ cannot be derived analytically due to the severe nonlinearity of the equation. Therefore, a sufficient-order polynomial function is used to estimate the anonymous function:

$$\hat{f}(x) = 0 \tag{30}$$

Then based on the nonlinear transformation [21], a 2-order polynomial is taken as an example to approximate the function:

$$\hat{f}(x)=\sum_{i=1}^{n_{tr}}\alpha_i(x_{1i}^2x_1^2+x_{2i}^2x_2^2+2x_{1i}x_{2i}x_1x_2+2x_{1i}x_1+2x_{2i}x_2+1)$$
$$=\alpha_1(x_{11}^2x_1^2+x_{21}^2x_2^2+\cdots+1)+\cdots+\alpha_{n_{tr}}(x_{1n_{tr}}^2x_1^2+x_{2n_{tr}}^2x_2^2+\cdots+1)$$
$$=c_1x_1^2+c_2x_2^2+c_3x_1x_2+c_4x_1+c_5x_2+c_6 \tag{31}$$

where n_{tr} is the size of the training set; x_1 and x_2 are the variables in the parameter space; $c_1 \sim c_6$ are the corresponding coefficients for each term of the 2-order polynomial function. This result can be generalized into h-order polynomial function. For example, there are nine coefficients for 3-order polynomial function and 15 coefficients for 4-order polynomial function.

In (31), the coefficient α is calculated as:

$$\alpha=(K+\lambda I)^{-1}\sigma_{\max} \tag{32}$$

where $\sigma_{\max} = [\sigma_{\max\_1}, \sigma_{\max\_2}, \dots, \sigma_{\max\_n_{tr}}]^T$, and K is a matrix with its element calculated by $K_{i,j} = (x_i^T x_j + 1)^h$; I is an identity matrix with dimension n_{tr}; λ is estimated from the initial parameter settings $\lambda_{\min}$ and $\lambda_{\max}$, which separately correspond to the minimum eigenvalue and the maximum eigenvalue of matrix K.

Therefore, the training set separated from the generated dataset is used to determine coefficients in (31), which is used to approximate the original stability region boundary in (30).

C. Performance Verification

Based on the validation set, the derived approximate stability boundary can be validated by calculating the root-mean-square error (RMSE):

$$\text{RMSE}=\sqrt{\frac{1}{n_{va}}\sum_{i=1}^{n_{va}}\gamma_i^2} \tag{33}$$

where n_{va} is the size of the validation set; γ_i is the error between the estimated function in (6) and the value of the $\sigma_{\max}$.

Further, to estimate the polynomial order h, a simple method is that increasing the value of order h while searching for the optimal λ in the interval $\{\lambda_{\min}\ \lambda_{\max,}\}$ until (33) is smaller than a given threshold. In general, the error band is less than 5%. Additionally, if the validation error is less than a required threshold, the derived stability region boundary is satisfactory.

IV. Case Studies

As shown in Fig. 3., a 10-bus test system of an autonomous and hybrid AC and DC MG is comprised of two DGs, two loads and one line in the AC subsection, two DGs, two loads and one line in the DC subsection, as well as one interface inverter between AC and DC buses.

Case I: Stability Boundary with Parameter Space $\{L_{cdc}, R_{vac}\}$

By selecting the physical inductance L_{cdc} in the DC subsection and the virtual resistance R_{vac} in the AC subsection to establish a parameter space $\{L_{cdc}, R_{vac}\}$, a stability region is derived following the steps below. First, the dataset with 82 samples is generated based on the parameter space $\{L_{cdc}, R_{vac}\}$. Second, the sizes of the training set and the validation set are set to 50% of the retained samples, and the sample points are randomly selected. Third, the approximate stability boundary, as well as the corresponding four-order approximate boundary given by the KRR method, is shown in Fig. 4. Finally, in this case, the RMSE is calculated as 0.59% using the validation set, which satisfies our required threshold. In the meanwhile, Points A and B are selected as two examples, which indicate stable and unstable operation conditions, respectively. Their corresponding time-domain simulation waveforms are shown in Fig. 5, which are in accordance with operating conditions shown in the stability region in Fig. 4.

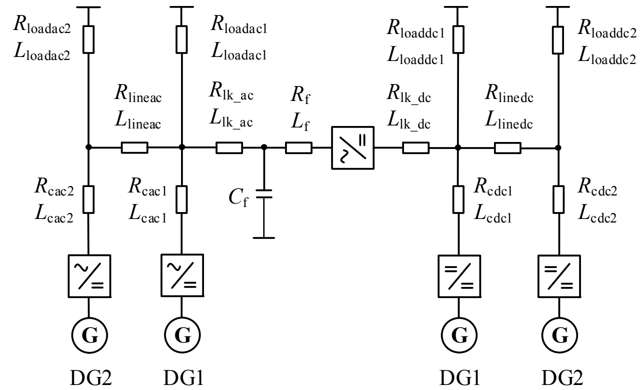

Fig. 3. Test system under case studies.

Case II: Stability Boundary with Parameter Space $\{R_{vac}, k_{pv}\}$

Similarly, the parameter space in Case II is comprised of virtual resistance R_{vac} in the AC subsection and the proportional gain k_{pv} of the outer DC-link voltage loop of interlink inverter. Then the dataset formed with 90 samples is used for deriving the stability boundary and its fourth-order approximation, as shown in Fig. 6. The RMSE is eventually computed as 1.39% in this case. Additionally, Point A and B are selected as two instances to indicate stable and unstable operation conditions, respectively. Their corresponding simulation test results in terms of operating conditions are following the theoretical region-based stability analysis, as shown in Fig. 7.

V. Conclusion

In this study, a holistic small-signal model of a hybrid AC/DC MG is established combining AC subsection, DC subsection, and interlink inverters. Additionally, the stability margin of the obtained model is identified by using the proposed region-based stability approach considering the selected cross-domain parameter space with elements from either the control diagram or the main power circuit. As an AI-assisted and computationally efficient approach, the KRR algorithm is employed to estimate the stability boundary. The proposed framework and method are verified using time-domain simulation tests.

Acknowledgment

This material is based upon work supported by the U.S. Department of Energy's Office of Energy Efficiency and Renewable Energy (EERE) under the Solar Energy Technologies Office award (Award Number: 34225).

References

[1] F. Nejabatkhah and Y. W. Li, "Overview of Power Management Strategies of Hybrid AC/DC Microgrid," *IEEE Trans. Power Electron*., vol. 30, no. 12, pp. 7072-7089, 2015.

[2] X. Liu, P. Wang and P. C. Loh, "A Hybrid AC/DC Microgrid and Its Coordination Control," *IEEE Trans. Smart Grid*, vol. 2, no. 2, pp. 278-286, June 2011.

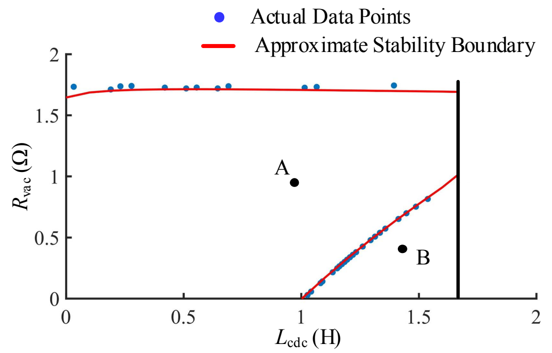

$$0.126L_{cdc}^4 + 0.826R_{vac}^4 + 2.787L_{cdc}^3 R_{vac} - 3.093L_{cdc}^2 R_{vac}^2 - 0.853L_{cdc} R_{vac}^3 - 5.411L_{cdc}^3 - 1.375R_{vac}^3 - 0.928L_{cdc}^2 R_{vac} + 8.278L_{cdc} R_{vac}^2 + 11.744L_{cdc}^2 - 2.3R_{vac}^2 - 10.22L_{cdc} R_{vac} - 3.187L_{cdc} + 5.82R_{vac} - 3.282 = 0$$

Fig. 4. Approximate stability boundary (red) and sample points along the boundary (blue) in the parameter space $\{L_{cdc}, R_{vac}\}$.

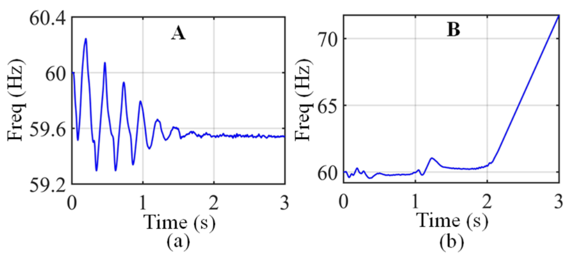

Fig. 5. Time-domain waveforms of Point A and Point B.
(a) Stable operation condition; (b) Unstable operation condition.

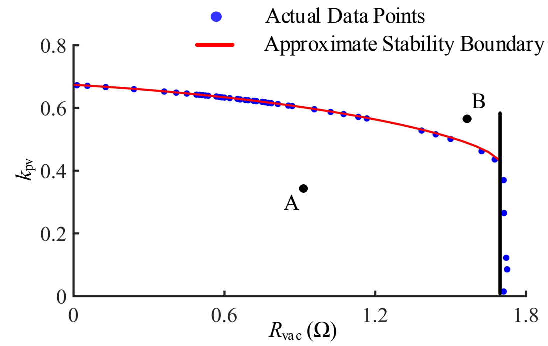

$$-0.144R_{vac}^4 + 5.926k_{pv}^4 - 0.105R_{vac}^3 k_{pv} - 9.153R_{vac}^2 k_{pv}^2 - 4.521R_{vac} k_{pv}^3 - 0.281R_{vac}^3 + 4.971k_{pv}^3 + 6.126R_{vac}^2 k_{pv} + 10.383R_{vac} k_{pv}^2 + 0.672R_{vac}^2 + 9.196k_{pv}^2 - 6.313R_{vac} k_{pv} + 1.837R_{vac} - 6.58k_{pv} - 2.485 = 0$$

Fig. 6. Approximate stability boundary (red) and sample points along the boundary (blue) in the parameter space $\{R_{vac}, k_{pv}\}$.

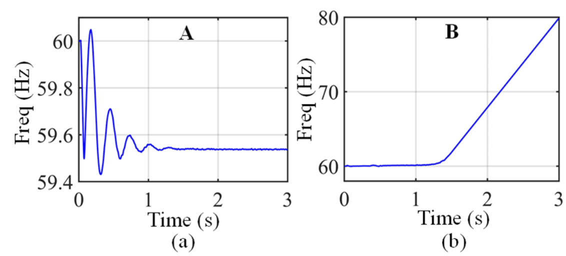

Fig. 7. Time-domain waveforms of Point A and Point B.
(a) Stable operation condition; (b) Unstable operation condition.

[3] J. Rajagopalan, K. Xing, Y. Guo, and F. C. Lee, “Modeling and dynamic analysis of paralleled dc/dc converters with master-slave current sharing control,” in *Proc. IEEE Appl. Power Electron. Conf.*, pp. 678–684, 1996.

[4] A. P. Martins, A. S. Carvalho, and A. S. Araújo, “Design and implementation of a current controller for the parallel operation of standard USPs,” in *Proc. IEEE IECON*, pp. 584–589, 1995.

[5] J. M. Guerrero, L. G. de Vicuna, J. Matas, M. Castilla and J. Miret, "A wireless controller to enhance dynamic performance of parallel inverters in distributed generation systems," *IEEE Trans. Power Electron.*, vol. 19, no. 5, pp. 1205-1213, Sept. 2004.

[6] Y. W. Li and C. Kao, "An Accurate Power Control Strategy for Power-Electronics-Interfaced Distributed Generation Units Operating in a Low-Voltage Multibus Microgrid," *IEEE Trans. Power Electron.*, vol. 24, no. 12, pp. 2977-2988, Dec. 2009.

[7] Q. Zhong and G. Weiss, "Synchronverters: Inverters That Mimic Synchronous Generators," *IEEE Trans. Ind. Electron.*, vol. 58, no. 4, pp. 1259-1267, April 2011.

[8] J. M. Guerrero, J. C. Vasquez, J. Matas, L. G. de Vicuna and M. Castilla, "Hierarchical Control of Droop-Controlled AC and DC Microgrids—A General Approach Toward Standardization," *IEEE Trans. Ind. Electron.*, vol. 58, no. 1, pp. 158-172, Jan. 2011.

[9] X. Lu, J. M. Guerrero, *et al*, "Hierarchical Control of Parallel AC-DC Converter Interfaces for Hybrid Microgrids," *IEEE Trans. Smart Grid*, vol. 5, no. 2, pp. 683-692, March 2014.

[10] V. Nasirian, S. Moayedi, A. Davoudi and F. L. Lewis, "Distributed Cooperative Control of DC Microgrids," *IEEE Trans. Power Electron.*, vol. 30, no. 4, pp. 2288-2303, April 2015.

[11] Y. Du, X. Lu, J. Wang and S. Lukic, "Distributed Secondary Control Strategy for Microgrid Operation with Dynamic Boundaries," *IEEE Trans. Smart Grid*, vol. 10, no. 5, pp. 5269-5282, Sept. 2019.

[12] Y. Du, X. Lu, H. Tu, J. Wang and S. Lukic, "Dynamic Microgrids with Self-Organized Grid-Forming Inverters in Unbalanced Distribution Feeders," *IEEE J. of Emerging and Selected Topics in Power Electron.*, vol. 8, no. 2, pp. 1097-1107, June 2020.

[13] Y. Du, X. Lu, *et al*, "Dynamic Microgrids in Resilient Distribution Systems with Reconfigurable Cyber-Physical Networks," *IEEE J. of Emerging and Selected Topics in Power Electron.*, 2020.

[14] H. Tu, Y. Du, *et al*, "Resilient Information Architecture Platform for the Smart Grid (RIAPS): A Novel Open-Source Platform for Microgrid Control," *IEEE Trans. Ind. Electron.*, 2019.

[15] Z. Li and M. Shahidehpour, “Small-Signal Modeling and Stability Analysis of Hybrid AC/DC Microgrids,” *IEEE Trans. Smart Grid*, vol. 10, no. 2, pp. 2080-2095, 2019.

[16] N. Pogaku, M. Prodanovic and T. C. Green, “Modeling, analysis and testing of autonomous operation of an inverter-based microgrid,” *IEEE Trans. Power Electron.*, vol. 22, no. 2, pp. 613–625, March 2007.

[17] S. Anand and B. G. Fernandes, “Reduced-Order Model and Stability Analysis of Low-Voltage DC Microgrid,” *IEEE Trans. Ind. Electron.*, vol. 60, no. 11, pp. 5040-5049, 2013.

[18] Y. Pan, S. Mei, *et al*, “Admissible Region of Large-Scale Uncertain Wind Generation Considering Small-Signal Stability of Power Systems,” *IEEE Trans. Sust. Energy*, vol. 7, no. 4, pp. 1611-1623, Oct. 2016.

[19] Y. Guo, L. Chen, *et al*, "Region-Based Stability Analysis for Active Dampers in AC Microgrids," *IEEE Trans. Ind. Appl.*, vol. 55, no. 6, pp. 7671-7682, Nov.-Dec. 2019.

[20] F. Mumtaz, M. H. Syed, M. A. Hosani and H. H. Zeineldin, "A Novel Approach to Solve Power Flow for Islanded Microgrids Using Modified Newton Raphson With Droop Control of DG," *IEEE Trans. Sust. Energy*, vol. 7, no. 2, pp. 493-503, April 2016.

[21] B. Jayasekara and U. D. Annakkage, "Derivation of an Accurate Polynomial Representation of the Transient Stability Boundary," *IEEE Trans. Power Syst.*, vol. 21, no. 4, pp. 1856-1863, Nov. 2006.